The Planetary Science Journal, 7:169 (15pp), 2026 July https://doi.org/10.3847/PSJ/ae7e6f

Planet-wide, Concentric Density Waves in Venus's Upper Atmosphere Revealed through Polarimetry?

Gourav Mahapatra[1], Michiel Rodenhuis[2], Frans Snik[2], Daphne M. Stam[2], Loïc Rossi[1], and Christoph Keller[2,3]
[1] Faculty of Aerospace Engineering, Delft University of Technology, Delft, The Netherlands; mahapatra.gourav@gmail.com
[2] Leiden Observatory, Leiden University, Leiden, The Netherlands
[3] National Solar Observatory, 3665 Discovery Drive, Boulder, CO 80303, USA
Received 2025 November 7; revised 2026 May 26; accepted 2026 June 14; published 2026 July 9

Abstract

We report observations of faint (10^{-6}), concentric, planet-wide rings in the polarized flux of sunlight that is reflected by Venus, obtained during a serendipitous, 36-minute run in 2010, with the highly sensitive Extreme Polarimeter (ExPo) on the William Herschel Telescope. The rings appear to be centered slightly downwind of the subsolar point, are visible in different filters across the visible, and are not obvious in the simultaneous total flux observations. ExPo's dual-beam exchange and double-differencing design strongly suppresses first-order instrumental polarization, and we could not identify an instrumental cause of the observed pattern. Because ExPo was dismantled before the rings were identified in the data, this is the only set of observations of these rings. We are therefore careful in claiming the detection of a new atmospheric phenomenon on Venus. However, numerical radiative transfer simulations show that planet-wide rings in polarization can arise owing to density variations of 5%–10% in the gas above the clouds, consistent with a gravity wave. Our simulations also show that such density variations would not show up in total flux observations. By presenting our observations and numerical simulations, we hope to motivate new polarimetric observations of Venus that could confirm or refute the presence of such planet-wide waves.

Unified Astronomy Thesaurus concepts: Venus (1763); Polarimetry (1278); Spectropolarimetry (1973); Radiative transfer (1335); Planetary atmospheres (1244); Atmospheric dynamics (2300)

1. Introduction

There is ample evidence for gravity-wave activity on Venus. Indeed, waves with various wavelengths have been observed through direct imaging (e.g., Venus Express and Akatsuki images), as well as through in situ measurements (W. Kasprzak et al. 1988; A. Migliorini et al. 2011; A. Piccialli et al. 2014; J. Peralta et al. 2017; M. Persson et al. 2026). The properties of gravity waves depend on the atmospheric structure and on the thermal and dynamical interactions within the atmosphere. A recent example of planet-wide wave interaction is the bow-shaped planet-wide gravity wave detected by the Akatsuki spacecraft just after it entered into the orbit around Venus. These waves were topographic gravity waves, generated by near-surface flows impinging on mountains and propagating upward. Since these waves possess momentum in the direction opposite to Venus's superrotation, their dissipation at high altitudes exerts deceleration on the mean flow velocity (T. Kitahara et al. 2019). Venus's middle and upper atmosphere has long been expected to support gravity waves with wavelengths ranging from 100 to 600 km (W. Kasprzak et al. 1988). It has been conjectured that wave drag and turbulence due to such internal gravity waves propagating in Venus's upper atmosphere are critical to understanding its superrotation (M. Alexander 1992; M. Alexander et al. 1993). Detecting and characterizing them on both Venus's dayside and nightside would improve our understanding of our still enigmatic neighboring planet's dynamic atmosphere.

The density variations in the thin atmosphere above the clouds will be quite small and very challenging to detect with flux measurements of, e.g., reflected sunlight, in particular because the bright, underlying clouds will completely dominate the signal. Polarimetry could facilitate the detection of subtle atmospheric density changes in the upper atmosphere of Venus because of its higher sensitivity through the process of Rayleigh scattering by the gas molecules.

This article presents ground-based imaging polarimetry of Venus at various visible wavelengths using the Extreme Polarimeter (ExPo) instrument (M. Rodenhuis & C. U. Keller 2007; H. Canovas et al. 2011). We investigate an apparent ringlike polarization pattern in a unique serendipitous dataset and explore whether it could plausibly be explained by gas-density variations above the cloud tops. ExPo is an experimental instrument developed to provide high-contrast imaging polarimetry, with the primary objective of observing weak sources, such as exoplanets, in reflected (and thus linearly polarized) starlight at small angular separations from their host stars. The instrument is highly sensitive to linearly polarized light, capable of achieving a sensitivity of 10^{-4} provided that sufficient photons are available (M. Rodenhuis et al. 2008). Because the observations are limited to a single serendipitous dataset and cannot be repeated with the same instrument, our goal is not to claim a definitive detection of a new Venusian wave phenomenon but to assess whether the observed pattern is physically plausible and worthy of targeted future observations.

In Section 2, we describe the observations. In Section 3, we outline the observational and numerical methods employed in this study, including definitions of polarized light observations (Section 3.1), a description of the instrument (Section 3.2), and the radiative transfer algorithm (Section 3.3). Section 4 provides a discussion of the observations, while Section 5

Table 1
Overview of the Venus Observations Obtained with ExPo on the WHT, La Palma, Spain on 2010 May 24

Filter	λ_0 (nm)	$\Delta\lambda$ (nm)	θ (deg)	Time (UTC)	Elevation (deg)	Air Mass	Rings Visible
Hα	656.3	1.0	45.0	20:28:18	24.06	2.438	yes
			67.5	20:31:03	23.43	2.499	yes
Hα cont.	647.1	1.0	0.0	20:33:45	22.80	2.541	yes
			22.5	20:39:14	21.75	2.678	yes
			45.0	20:41:33	21.34	2.727	yes
			67.5	20:43:59	20.71	2.778	yes
Na	589.4	5.0	45.0	20:51:38	19.05	3.003	yes
			67.5	20:54:01	18.63	3.097	yes
Na cont.	580.0	5.0	45.0	21:03:19	16.77	3.419	no
			67.5	21:06:30	16.16	3.542	no
Sloan r	623.1	137.3	45.0	21:23:30	12.68	4.449	no
			67.5	21:25:39	12.07	4.586	no
Sloan i	762.5	152.6	45.0	21:32:21	10.85	5.139	no
			67.5	21:34:31	10.45	5.322	no

Note. During our observations, Venus's phase angle was 48.°7, and its angular diameter was 12.″5 (outside Earth's atmosphere). The technical parameters of the observations are listed below. For each filter, we give the central wavelength λ_0 and bandwidth $\Delta\lambda$. And for each observation: the angle θ of ExPo's FLC, the time, Venus's elevation and air mass, and the visibility of the rings in the polarized flux. Venus's angular diameter and air mass at the times of the observations were obtained using JPL's Horizons ephemeris tool.

examines the observations in conjunction with the results of the radiative transfer model and their implications.

2. The Observations

The Venus images we present here are truly serendipitous: they were captured with ExPo as it was installed at the Nasmyth focus of the 4.2 m William Herschel Telescope (WHT) of the Isaac Newton Group (ING) of telescopes on La Palma, Canary Islands, Spain, during a period of about 36 minutes in which we were waiting for the end of the astronomical evening twilight on 2010 May 24 to start observations of circumstellar disks. The images were taken through six optical filters present in the instrument filter wheel: Hα, Hα continuum, Na continuum, Sloan r, Sloan i, and Na. The filter specifications and the times at which they were used are listed in Table 1. ExPo was designed to capture images of faint, linearly polarized sources by suppressing the contributions of unpolarized light to a high degree (M. Rodenhuis et al. 2012). The seeing on the evening of the observations (2010 May 24) was excellent (0.″8 or better), although the horizon where Venus was observed during the last observations just before setting appeared to be hazy, possibly leading to increased atmospheric seeing values. The absolute accuracy of these impromptu images (and thus the background polarization level) can only be calibrated to 1%–2%. This, however, is no limitation for their interpretation because ExPo has been designed to reach a very high polarimetric sensitivity of 10^{-4}.

Figure 1 shows Venus in total (left) and linearly polarized (right) fluxes as imaged through the Hα continuum filter (see Table 1). While the total-flux image shows a homogeneous planet that is brightest near the subsolar region, the polarization image shows relatively high polarized fluxes across the north and south polar regions, lower polarization at lower latitudes, and superimposed narrow, higher-polarization rings.[4] The high polarization across Venus's poles has been observed before, for example, by Orbiter Cloud Photopolarimeter (OCPP; L. D. Travis 1979) on the Pioneer Venus spacecraft (K. Kawabata et al. 1980; M. Sato et al. 1996) and by Spectroscopy for Investigation of Characteristics of the Atmosphere of Venus (SPICAV) on Venus Express (L. Rossi et al. 2015). It is worth noting that the Pioneer Venus OCPP had a polarimetric sensitivity of approximately 10^{-3} (D. M. Hunten et al. 2022), which is a magnitude lower than that of ExPo. The SPICAV-IR instrument on Venus Express, while capable of deriving partial polarization from orthogonally polarized flux measurements, was not specifically calibrated for polarimetric observations. Consequently, the exact polarimetric sensitivity of SPICAV-IR remains unknown. The pattern appears roughly concentric around a region slightly downwind of the subsolar point and extends across much of the illuminated disk. They were observed in the first three observations through the Hα, Hα continuum, and Na, but not in the later Na continuum, Sloan r, and Sloan i observations. The typical difference between the polarized flux inside and outside the brightest ring in the image in Figure 1 is 5×10^{-4}.

Figure 2 provides a more quantitative comparison between the total and polarized flux in the same Hα continuum observation shown in Figure 1. We extract a one-dimensional equatorial cut averaged over the latitude band $-5° \leqslant \text{lat} \leqslant +5°$, i.e., the same strip that is used later in the longitude-resolved comparison. Panel (a) shows that the total flux is dominated by the smooth limb-darkening profile and does not show a detectable coherent ring-scale modulation. Panel (b), by contrast, shows that the polarized flux U along the same strip exhibits a clear oscillatory pattern with amplitude of order $\sim 10^{-4} F_{\rm peak}$ on top of the slowly varying continuum polarization.

As detailed in Table 1, various other filters were used to observe Venus on the same day during this observation campaign. Figure 3 shows our six observations of Venus in polarized flux, which is defined as $\sqrt{Q^2 + U^2}$. In all images,

[4] Although we do not know whether all arcs form full rings across the planet, we will refer to them as "rings."

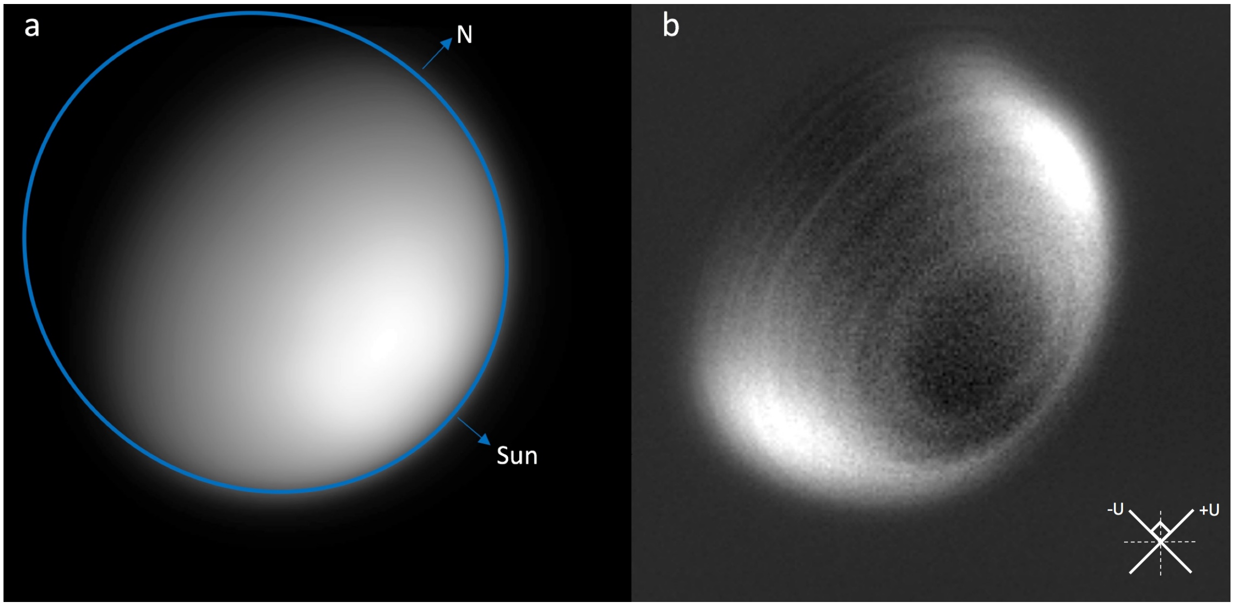

Figure 1. Venus as observed in total flux F (left) and polarized flux U (right) through the Hα continuum filter (see Table 1). Due to Venus's orientation, the planetary scattering plane makes an angle of about 45° with ExPo's optical plane (the two orthogonal directions along which ExPo measured U are indicated below the image). The spatial resolution is approximately 775 km at the subobserver point on Venus's disk.

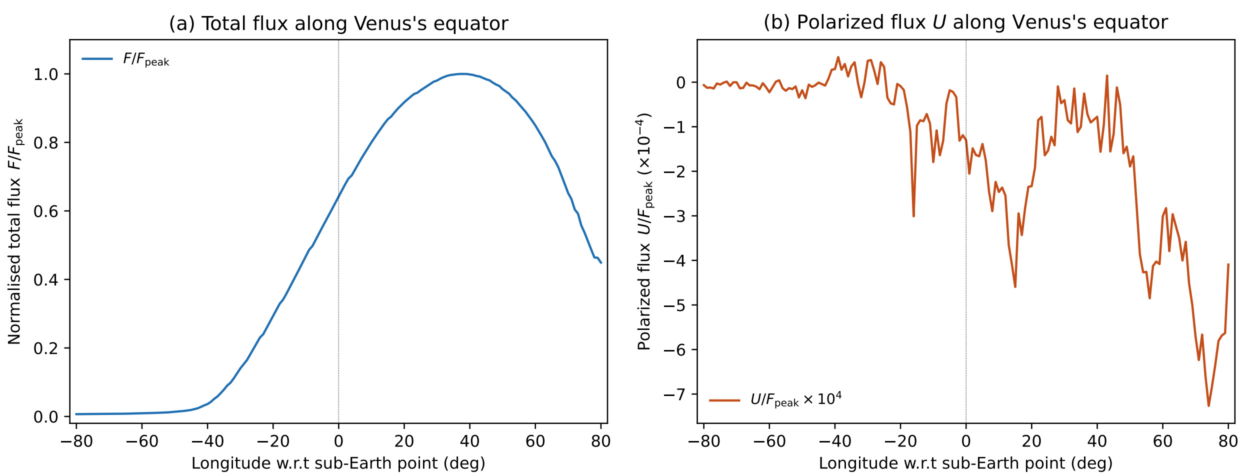

Figure 2. Equatorial cut through the Hα continuum observation shown in Figure 1, averaged over latitudes $-5° \leqslant$ lat $\leqslant +5°$. (a) Total flux F/F_{peak} as a function of subobserver longitude. (b) Polarized flux U/F_{peak} along the same strip, scaled by 10^4 for readability. The total-flux cut shows no coherent ring-scale modulation, whereas the polarized-flux cut exhibits the structure corresponding to the ringlike pattern visible in the polarized image of Figure 1.

Venus shows a similar background polarized flux that is small in the equatorial region and high toward the poles.

Three of the images (obtained through the Hα, Hα cont., and Na filters) show concentric ringlike patterns, while three (obtained through the Na cont., Sloan *r*, and Sloan *i* filters) do not. The latter three observations were obtained later in the sequence (see Table 1), when Venus was lower on the horizon and the air mass was larger. However, the visibility of the features does not show a simple monotonic dependence on air mass alone: the Na observation at 589.4 nm, obtained after the Hα and Hα continuum observations and at somewhat higher air mass, still shows a particularly clear pattern. This indicates that increased air mass and reduced spatial resolution cannot by themselves explain the detect versus nondetect behavior. Instead, the observations are more likely shaped by a combination of effects, including wavelength-dependent sensitivity of the polarization signal, atmospheric seeing, and the lack of an operational atmospheric dispersion corrector in ExPo during these observations, which may have introduced some spectral smearing in the broader filters.

Figure 4 shows the degree of polarization U/F for the six observations, except only for the latitudes between −30° and +30°, as functions of the longitude on the planet measured with respect to the subobserver or sub-Earth point. The blue line in each panel shows the degree of polarization averaged between latitudes −5° and +5°. The modulation due to ringlike patterns can be seen in the blue lines in the upper three panels, which pertain to the observations that were taken first, and not in the lowest three panels, which pertain to the observations that were taken last. The strength of the ring pattern varies from filter to filter. In particular, the relatively strong visibility of the patterns in the Na filter at 589.4 nm,

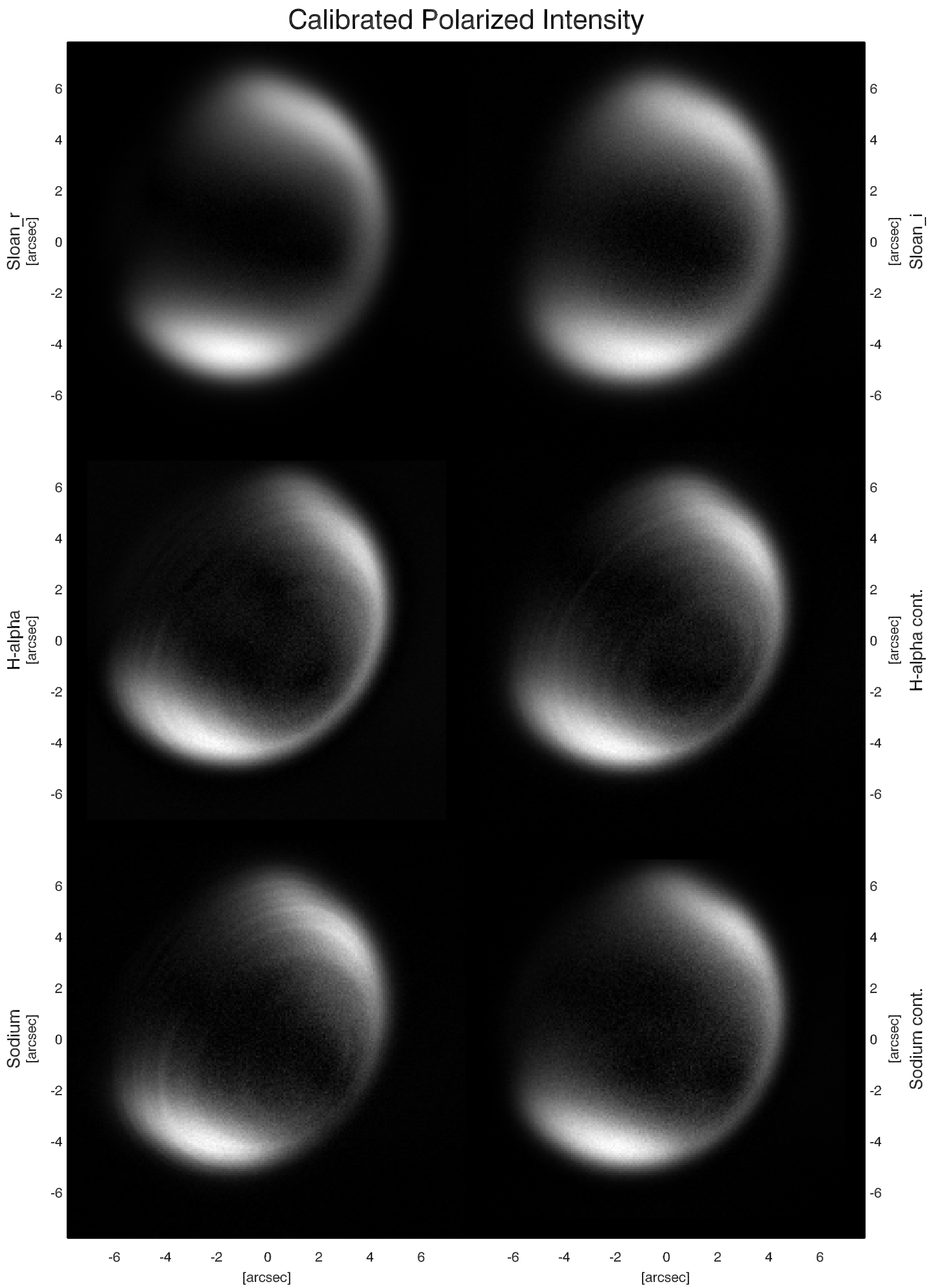

Figure 3. The polarized flux ($\sqrt{Q^2 + U^2}$) as measured through the six filters (see Table 1). Top row: the Sloan *r* and Sloan *i* broadband filters. Middle row: the Hα and Hα continuum filters. Bottom row: the Na (sodium) and Na continuum filters. The time sequence of the observations is from top left to bottom right: 5–6–1–2–3–4. The ringlike pattern is apparent in the first three observations in chronological order (1, 2, 3) and not obvious in the last three (4, 5, 6). Notably, the Na image at 589.4 nm still shows a clear ring pattern despite having been obtained at higher air mass than the Hα and Hα continuum observations.

compared with the Hα and Hα continuum filters at longer wavelengths, is qualitatively consistent with the model prediction that the sensitivity of the polarization signal to gas-density variations increases toward shorter wavelengths because of stronger Rayleigh scattering (see Section 4.1). At the same time, the observations do not follow a purely wavelength-driven sequence, indicating that observing conditions, including atmospheric seeing and air mass, could have played an important role. This is not surprising because, already during the first observations (through the Hα filter), Venus had an elevation of only about 24° and thus low on the hazy horizon (see Section 5 for the effect of variation in

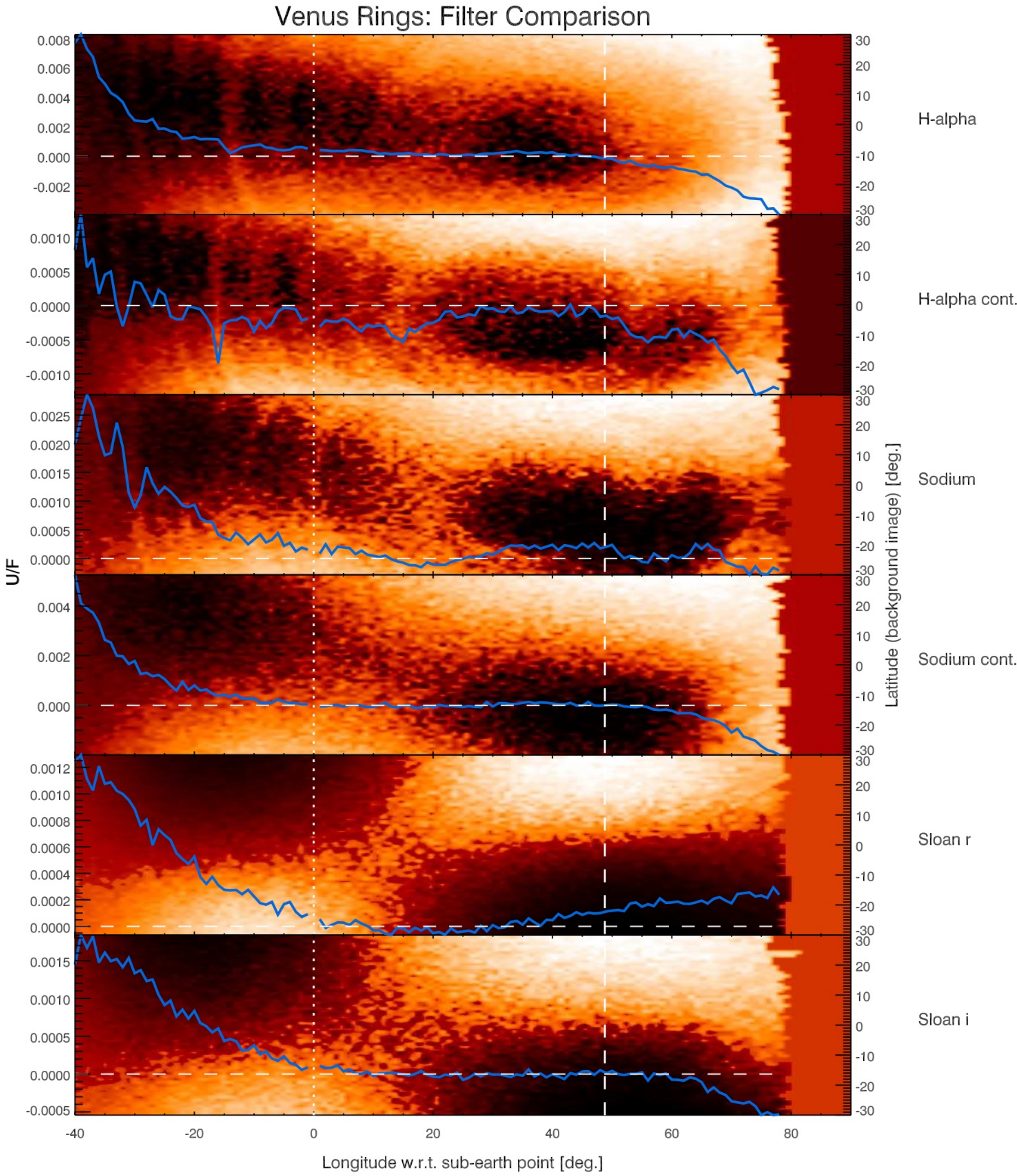

Figure 4. The background (red-orange) shows the degree of polarization as a function of longitude with respect to the subobserver point (horizontal axis) and the latitude from $-30°$ to $+30°$ on Venus (vertical axis) as measured in the various filters, with the time of observation increasing from top to bottom (see Table 1). The blue line shows the degree of polarization averaged over the latitudes between $-5°$ and $+5°$ as a function of longitude with respect to the subobserver point (scale on the left). The degree of polarization equals *U/F*, with *U* defined with respect to the instrumental optical plane. Because the orientation of the planet with respect to this plane is almost equal to 45°, Stokes parameter *U* in the instrumental optical plane corresponds almost to Stokes parameter *Q* in the planetary scattering plane. The difference between the planetary scattering plane and the instrumental optical plane is 3°–5°. The patterns are less visible in Stokes parameter *Q* defined with respect to the instrumental optical plane (and hence they are much less visible in Stokes parameter *U* as defined with respect to the planetary scattering plane), indicating that the direction of polarization of the background signal and the rings is mostly parallel to the planetary scattering plane (see Figure 5). The vertical dotted line indicates the subobserver or sub-Earth longitude, and the vertical dashed line indicates the subsolar longitude. The horizontal long-dashed line indicates the zero polarization level for the blue lines. Note that because of the lack of accurate absolute calibration, this blue line and the zero level have an uncertainty of 1%–2%. The shape of the continuum polarization is also influenced by the difference between the planetary scattering plane and the instrumental optical plane.

atmospheric seeing). ExPo was an experimental instrument that underwent continuous development and modification. It was never reinstalled on the telescope in an identical configuration and has since been decommissioned.

The strong feature at longitudes of about $-12°$ in the observations through the Hα filter appears to also have been captured in the observations through the Hα cont. filter, except somewhat closer toward the terminator. The time interval between these observations was about 10 minutes (see Table 1). It is tempting to derive a speed of a density wave, assuming that it is indeed the same feature, but because of the lack of continuous observations and without any knowledge on the variability of the pattern in strength and location, one should indeed be careful using this for the characterization of the phenomenon.

Finally, Figure 5 shows the direction of polarization as derived from the observations through the Hα cont. filter. The direction is mostly parallel to the planetary scattering plane

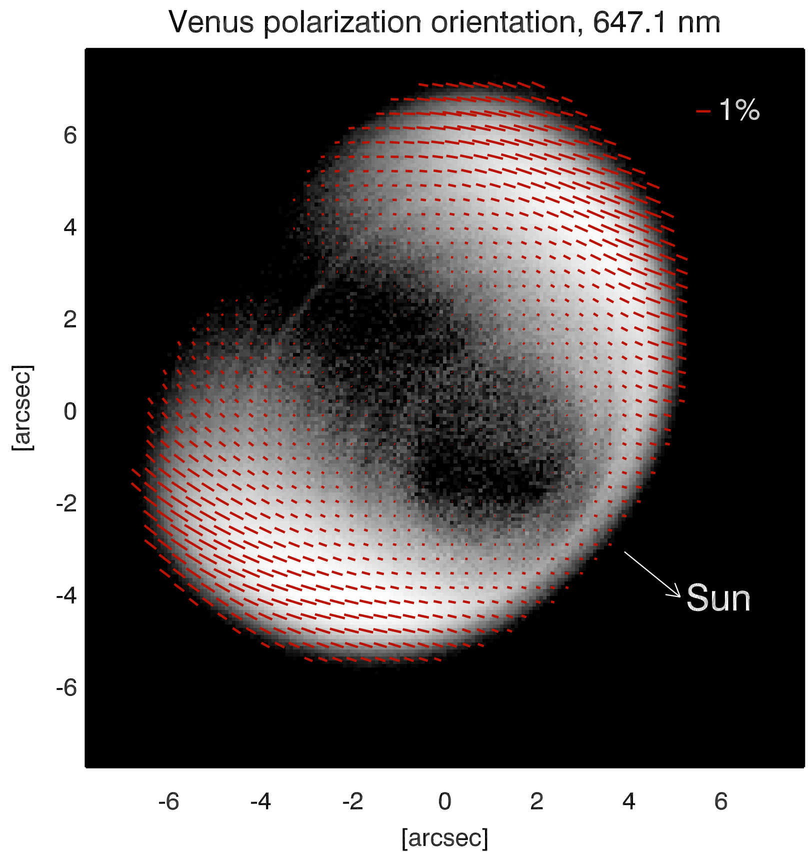

Figure 5. The direction of polarization as measured using the Hα cont. filter ($\lambda_0 = 647.1$ nm). The orientation of the red lines indicates the polarization direction (note that the direction is not shown for every pixel to avoid cluttering), and the line length indicates the local degree of polarization, which is predominantly determined by the polarization signal of the lower atmospheric layers that contain the hazes and clouds.

and thus to the equator of the planet. The direction does not show deviations related to the rings, which corresponds with the results of our numerical simulations (see Section 4.1), in which the polarization continuum is negative, hence parallel to the reference plane. An increased gas density above the clouds and hazes will force the degree of polarization closer to zero, but P remains negative.

The direction of polarization across the disk in Figure 1 is mostly parallel to the planetary scattering plane, without a significant change of the direction of polarization across the rings (see Figure 5). The rings appear in the images taken in the Hα, Hα continuum, and Na filters, which were taken first during the excellent seeing conditions. In the images taken in the Na continuum, Sloan r, and Sloan i filters, the polarization across the poles is still high and that at low latitudes is still low, but there are no rings distinguishable within ExPo's sensitivity. We have no other images of Venus with rings, as we did not have other opportunities to observe Venus under such advantageous seeing conditions and, due to the experimental nature of ExPo, the instrument has been taken apart and its optical components reused for other experiments. To the best of our knowledge, there are no other polarimeters available that combine imaging with ExPo's high polarimetric sensitivity.

As these rings have not been observed before, we first suspected them to be due to an instrumental effect, in particular because they appear to be roughly concentric around the brightest region on Venus's disk. However, ExPo was specifically designed to suppress instrumental polarization and other first-order systematic effects through its dual-beam exchange technique (Section 3.2), in which the signal is switched between two orthogonally polarized channels and recovered through double differencing. We have not been able to identify an instrumental effect that would leave rings in the images taken in the Hα, Hα continuum, and Na filters and not in the other filters. Nor can we identify a plausible mechanism by which filter-induced polarization alone, including in the narrowband filters, would produce the observed large-scale, spatially coherent ring pattern centered near the subsolar point on Venus's disk. If the filters were the dominant cause of the signal, such a geometrically organized morphology would not be expected. Moreover, similar features have not appeared in any other high-precision polarization images taken with ExPo (S. Jeffers et al. 2012; M. Rodenhuis et al. 2012; M. Min et al. 2013), nor have they appeared in carefully executed optical laboratory measurements with ExPo, including tests using a white styrofoam ball to simulate Venus. We also considered optical effects in Earth's atmosphere, such as scattering by an optically thin layer of high-altitude ice particles, but failed to find an explanation for the shape and location of the pattern on Venus, for the stability of the pattern during the observations through the first three filters, and especially for the consistent direction of polarization across Venus's disk and the rings.

Although we have not identified a plausible instrumental explanation for the pattern, the present data do not allow us to exclude an unknown artifact completely. If the candidate signal is astrophysical, scattering of sunlight within Venus's atmosphere provides a plausible explanation. The lack of a similarly apparent pattern in the last three filters (see Table 1) is more likely due to a combination of larger air mass, degraded seeing, wavelength-dependent sensitivity, and possible spectral smearing in the broader filters.

We have identified several explanations why such features would not have been observed before. First, while Venus has been observed with ground-based polarimeters before (J. E. Hansen & J. W. Hovenier 1974), those observations did not have a spatial resolution high enough to resolve any features on the planet's disk. Spatially resolved polarimetry of Venus was performed with OCPP (L. D. Travis 1979). The polarimetric accuracy of OCPP, however, was 10^{-3} in the 365–935 nm range (L. D. Travis 1979), which would have been insufficient to detect the ringlike patterns that we have observed. The SPICAV instrument on the European Space Agency's (ESA) Venus Express mission had polarimetric capabilities thanks to its opto-acoustic modulator (O. Korablev et al. 2012; L. Rossi et al. 2015), but it covered mostly near-infrared wavelengths, at which, as we will show later, the rings would have been virtually invisible. In addition, SPICAV's polarimetric accuracy was at most 10^{-3}. The Japanese Space Agency's (JAXA) Akatsuki mission, which has been orbiting Venus since 2015, unfortunately does not carry a polarimeter. South Korea's twin-CubeSat CLOVE mission is planned to observe Venus with polarimetric capabilities (Y. J. Lee 2024). Venspec-H on ESA's EnVision mission to Venus, currently scheduled for launch in 2032, will include spectropolarimetric capability, but only at near-infrared wavelengths (J. Helbert et al. 2019; E. Neefs et al. 2025).

This observational dataset has important limitations. It consists of a single serendipitous observing sequence, and no comparable ExPo observations of Venus are available. Although ExPo was designed for very high polarimetric sensitivity and to suppress first-order instrumental effects, the absolute polarization offset of these impromptu observations is only calibrated to the 1%–2% level. Moreover, ExPo was an experimental instrument that was not later reinstalled in an identical configuration and has since been dismantled. For these reasons, the present observations cannot by themselves establish a definitive detection of a new Venusian atmospheric phenomenon and should instead be viewed as a candidate signal that requires independent confirmation.

3. Observing and Modeling the Rings in Polarization

3.1. Definitions of Fluxes and Polarization

We describe light with a Stokes (column) vector $\boldsymbol{F}$ as follows (J. E. Hansen & L. D. Travis 1974):

$$\boldsymbol{F} = [F, Q, U, V], \tag{1}$$

with F the total flux, Q and U the linearly polarized fluxes, and V the circularly polarized flux, all in units of W m^{-2}. These fluxes all depend on the wavelength λ, and we will compute them per spectral filter. Regarding sunlight that is reflected by a planet, the circularly polarized flux V is very small (J. E. Hansen & L. D. Travis 1974; L. Rossi & D. M. Stam 2018), and it is not measured by ExPo. The linearly polarized fluxes Q and U are defined with respect to a reference plane, for which we choose the planetary scattering plane, i.e., the plane containing the centers of the Sun, Venus, and the observer.

The degree of linear polarization P is defined as

$$P = \frac{\sqrt{Q^2 + U^2}}{F}, \tag{2}$$

with $\sqrt{Q^2 + U^2}$ the total linearly polarized flux. While the degree of linear polarization P is independent of the reference plane used for Stokes parameters Q and U, the direction or angle of linear polarization, χ, does depend on that choice. Angle χ can be derived from

$$\tan 2\chi = U/Q. \tag{3}$$

The value of χ is chosen in the interval $[0°, 180°\rangle$ and such that $\cos 2\chi$ has the same sign as Q (J. E. Hansen & L. D. Travis 1974).

In case polarized flux U equals zero, we can employ an alternative definition of the degree of linear polarization that includes information about the direction of polarization, namely

$$P_s = -Q/F. \tag{4}$$

If $P_s > 0$, the direction of polarization is perpendicular to the reference plane, and if $P_s < 0$, it is parallel to the reference plane.

3.2. Expo Instrument Description

Polarimetry is a differential measurement technique: in a simple polarimeter, a polarizing beam splitter is used to split the light into its two orthogonally polarized components. Of each of these components, the flux is then measured. The difference of two such flux measurements yields the net linearly polarized flux of the incoming light along the orthogonal axes defined by the beam splitter. ExPo (M. Rodenhuis et al. 2008; H. Canovas et al. 2011) has been designed to avoid introducing systematic or temporal errors by using a dual-beam exchange measurement approach: the light is passed through a polarizing beam splitter, and the two orthogonal polarization states are measured simultaneously. In front of the beam splitter, a switchable half-wave plate can interchange the two polarization states between the two beams. In the second state, the two polarization states are measured again. This technique is depicted in Figure 6. A ferro-electric liquid crystal (FLC) modulator switches between the two states synchronously with the camera's 35 Hz frame rate, thus canceling first-order systematic errors due to optical path differences and reducing noise that is due to variations in atmospheric seeing between consecutive frames. This dual-beam exchange and double-differencing strategy strongly suppresses first-order instrumental polarization and makes it difficult for a static optical component, such as a filter, to imprint a coherent disk-wide polarization morphology on the final reduced images (H. Canovas et al. 2011).

Calling the two states A and B (see Figure 6) and denoting the two beams by L and R, the polarized flux is found through the double difference of four measurements:

$$Q = A_L - A_R - B_L + B_R. \tag{5}$$

Rotating the switchable half-wave plate by 22°.5 makes the polarimeter sensitive to polarization at 45° with respect to the first measurement, allowing the measurement of the U component of the Stokes vector. The polarized flux is again

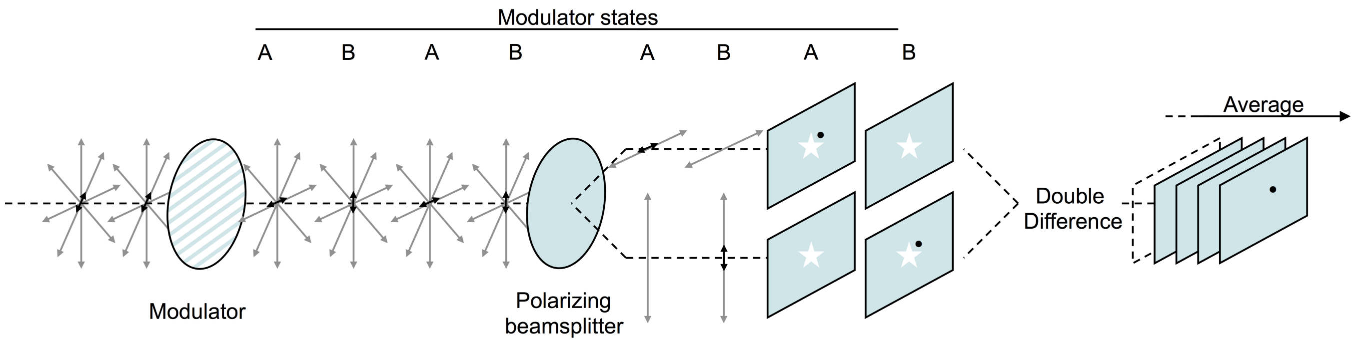

Figure 6. ExPo's dual-beam exchange polarimetry technique.

found through the double difference:

$$U = [A_L - A_R - B_L + B_R]^{45^\circ}. \tag{6}$$

ExPo was a regular instrument on the WHT, part of the Isaac Newton Group of telescopes on the island of La Palma, Spain. The WHT has an experimental instrument station at one of the Nasmyth ports, where a standard optical table is available on which such instruments can be mounted.

3.3. Radiative Transfer Algorithm

Our radiative transfer computations to reproduce the rings are based on an adding–doubling algorithm (J. F. de Haan et al. 1987) that fully includes linear and circular polarization for all orders of scattering. The algorithm requires a model atmosphere to be composed of a stack of horizontally homogeneous layers, and, for each of the layers, it requires the specification of the optical thickness b, the single-scattering albedo ω, and the single-scattering matrix $\boldsymbol{S}$ of the scattering particles in the layer. The atmosphere is bounded below by a horizontally homogeneous surface, which we assume to be black. The surface albedo is irrelevant for our simulations.

The optical thickness of an atmospheric layer at wavelength λ (D. Stam et al. 1999) is given by

$$b(\lambda) = b^m(\lambda) + b^a(\lambda), \tag{7}$$

with b^m the layer's gaseous optical thickness and b^a the layer's aerosol optical thickness, which is due to the cloud or haze particles (in our model atmosphere, a layer that contains aerosol contains either cloud or haze particles, not a mixture of both).

The single-scattering albedo in the layer is given by

$$\omega(\lambda) = \frac{\omega^m(\lambda)b^m(\lambda) + \omega^a(\lambda)b^a(\lambda)}{b^m(\lambda) + b^a(\lambda)}, \tag{8}$$

with ω^m the single-scattering albedo of the gas molecules and ω^a the single-scattering albedo of the cloud or haze particles in the layer. The single-scattering matrix of the particles in a layer is given by

$$\boldsymbol{S}(\lambda) = \frac{\omega^m(\lambda)b^m(\lambda)\boldsymbol{S}^m(\lambda) + \omega^a(\lambda)b^a(\lambda)\boldsymbol{S}^a(\lambda)}{\omega(\lambda)b(\lambda)}, \tag{9}$$

with $\boldsymbol{S}^m$ the single-scattering matrix of the gas and $\boldsymbol{S}^a$ the single-scattering matrix of the cloud or haze particles.

The single-scattering matrix $\boldsymbol{S}^m$ of anisotropic gaseous scattering and the depolarization factor $\delta(\lambda)$ is given by (J. E. Hansen & L. D. Travis 1974)

$$\boldsymbol{S}^m(\lambda, \Theta) = \Delta(\lambda) \times \begin{bmatrix} \frac{3}{4}(1+\cos^2\Theta) + \frac{1}{\Delta(\lambda)} - 1 & -\frac{3}{4}\sin^2\Theta & 0 & 0 \\ -\frac{3}{4}\sin^2\Theta & \frac{3}{4}(1+\cos^2\Theta) & 0 & 0 \\ 0 & 0 & \frac{3}{2}\cos\Theta & 0 \\ 0 & 0 & 0 & \Delta'(\lambda)\frac{3}{2}\cos\Theta \end{bmatrix}, \tag{10}$$

where

$$\Delta(\lambda) = \frac{1-\delta(\lambda)}{1+\delta(\lambda)/2} \text{ and } \Delta'(\lambda) = \frac{1-2\delta(\lambda)}{1-\delta(\lambda)}. \tag{11}$$

The four layers of our model atmosphere all contain pure carbon dioxide (CO_2) gas. In the filters that we used for our observations, CO_2 does not have any significant absorption bands. We thus neglect gaseous absorption in our computations, i.e., $\omega^m = 1.0$. The gas optical thickness, b^m, at a given wavelength λ of an atmospheric layer is then computed

Table 2
Parameters of Our Standard Venus Model Atmosphere

Layer	$p_{\rm bot}$ (bars)	$p_{\rm top}$ (bars)	N^m (m^{-2})	b^m (580 nm)	b^a (580 nm)
4	0.005	0.0	7.713E26	0.000794	0.0
3	0.05	0.005	6.942E27	0.00650	0.02
2	1.0	0.05	1.466E29	0.137	30.0
1	93.0	1.0	1.419E31	13.283	0.0

Note. The layers are listed from top to bottom. $p_{\rm bot}$ and $p_{\rm top}$ are the standard pressures at the bottom and top of each layer, respectively. N^m is the standard gas column number density based on the pressure range across each layer. b^m is the gaseous optical thickness of the layer at 580 nm, the central wavelength of the Na continuum filter (see Table 1), and b^a is the cloud or haze optical thickness of the layer, also at 580 nm. Layer 2 contains the cloud, and layer 3 contains the haze (see Table 3 for the values at other wavelengths). The single-scattering albedos of the gaseous molecules, ω^m, and those of the cloud and haze particles equal 1.0 in each layer and at each wavelength.

according to

$$b^m(\lambda) = N^m \sigma^m(\lambda), \tag{12}$$

with N^m the gas column number density (in m^{-2}) in the layer and σ^m the gaseous extinction cross section (in m^2), which in our case equals the gaseous scattering cross section, due to the lack of absorption. This cross section is given by

$$\sigma^m(\lambda) = \frac{24\pi^3}{N_{\rm L}^2} \frac{(n^2(\lambda)-1)^2}{(n^2(\lambda)+2)^2} \frac{(6+3\delta(\lambda))}{(6-7\delta(\lambda))} \frac{1}{\lambda^4}, \tag{13}$$

with $N_{\rm L}$ Loschmidt's number, n the refractive index of CO_2 under standard conditions, and δ the depolarization factor of pure CO_2. For n and δ of pure CO_2 gas, we assume the wavelength-dependent relations presented by M. Sneep & W. Ubachs (2005). It should be noted that the error in the equation for n by M. Sneep & W. Ubachs (2005) for CO_2 is ∼4%.

Assuming that each atmospheric layer is in hydrostatic equilibrium, a layer's gas column number density $N^{\rm m}$ (in m^{-2}) is computed using

$$N^{\rm m} = N_{\rm A} \frac{p_{\rm bot} - p_{\rm top}}{mg}, \tag{14}$$

with $N_{\rm A}$ Avogadro's number; $p_{\rm bot}$ and $p_{\rm top}$ the pressures at the bottom and at the top of the atmospheric layer, respectively; m the average molar mass of the gas, for which we use the value for pure CO_2, i.e., 44.01 g mol^{-1}; and g the acceleration of gravity, which we assume to be altitude independent across the region of Venus's atmosphere that we study and equal to 8.87 m s^{-2}. Table 2 shows the pressures at the bottom and the top of each of the four atmospheric layers that we use in our model, the computed gas column number density N^m, and the gaseous optical thickness b^m at 580 nm (the central wavelength of the Na cont. filter) for each of the atmospheric layers. We impose the variations in the gas column number density on the highest atmospheric layer. Thus, we impose a perturbation δN^m on the top layer, with a baseline gas column number density of $N^m = 6.942 \times 10^{27}$ m^{-2} (see Table 2), corresponding to the atmospheric column above the cloud tops.

The second and third layers of the model atmosphere contain, respectively, cloud and haze particles (see Table 2). These particles are assumed to be spherical and homogeneous. For both particle types, we assume a two-parameter gamma size distribution (J. E. Hansen & L. D. Travis 1974). The cloud particles have an effective radius $r_{\rm eff}$ of 1.05 μm and an effective variance $\nu_{\rm eff}$ of 0.07 (J. E. Hansen & J. W. Hovenier 1974), and for the haze particles, $r_{\rm eff} = 0.25$ μm and $\nu_{\rm eff} = 0.25$ (M. Sato et al. 1996). We assume that the cloud and haze particles consist of 75% sulfuric acid (J. E. Hansen & J. W. Hovenier 1974), and we adopt the following wavelength dependence for their refractive index n_r:

$$\frac{n_r^2(\lambda) - 1}{n_r^2(\lambda) + 2} = \frac{-29.8034}{\lambda^{-2} - 116.3899}, \tag{15}$$

as derived from the values provided by J. E. Hansen & J. W. Hovenier (1974).

For each central filter wavelength λ_0 (Table 1), we compute the optical properties of the cloud and haze particles, i.e., their extinction cross section σ^a and their single-scattering matrix $\boldsymbol{S}^a$, using a Mie algorithm (W. A. de Rooij & C. C. A. H. van der Stap 1984). Their single-scattering albedo ω^a equals 1.0 owing to the lack of absorption.

Figure 7 shows the total flux and degree of linear polarization of unpolarized incident light that is singly scattered by the cloud and haze particles for the central filter wavelengths λ_0. For comparison, we have also included the curves for the light that is scattered by the gaseous molecules. As can be seen, at a single-scattering angle of 131°.3, which corresponds to Venus's phase angle of 48°.7 at the time of the ExPo observations, the light scattered by the cloud particles is polarized parallel to the reference plane (which would correspond to the planetary scattering plane, which also contains the planet's equator), while the light scattered by the gaseous molecules is polarized perpendicular to this plane. For the haze particles, the degree of polarization at this scattering angle is close to zero for most wavelengths shown in Figure 6, and their polarization direction is therefore effectively undefined; at 762.5 nm, however, it is weakly polarized perpendicular to the reference plane.

We choose the cloud and haze optical thickness, b^a, of atmospheric layers 2 and 3 according to previous Venus atmospheric models (K. Kawabata et al. 1980; L. Rossi et al. 2015). Table 2 lists the optical thickness b^a of each layer at 580 nm (which is the central wavelength λ_0 of the Na cont. filter). The cloud or haze optical thicknesses at other wavelengths are computed according to

$$b^a(\lambda) = b^a(580\ {\rm nm}) \frac{\sigma^a(\lambda)}{\sigma^a(580\ {\rm nm})}. \tag{16}$$

The values of b^a of the cloud ($b^a_{\rm cloud}$) and the haze ($b^a_{\rm haze}$) at the central filter wavelengths can be found in Table 3. The particle scattering properties at the other wavelengths are calculated using the Mie code as described earlier.

We assume that the sunlight that is incident on the planet is unpolarized (J. C. Kemp et al. 1987), and it is thus described by the column vector $F_0[1, 0, 0, 0]$, with F_0 equal to π.

To numerically simulate the observations, we represent Venus's disk with a grid of equally sized, square pixels. We projected the planetary disk onto the plane of the sky and divided the circumscribing square into a 300 × 300 grid, with

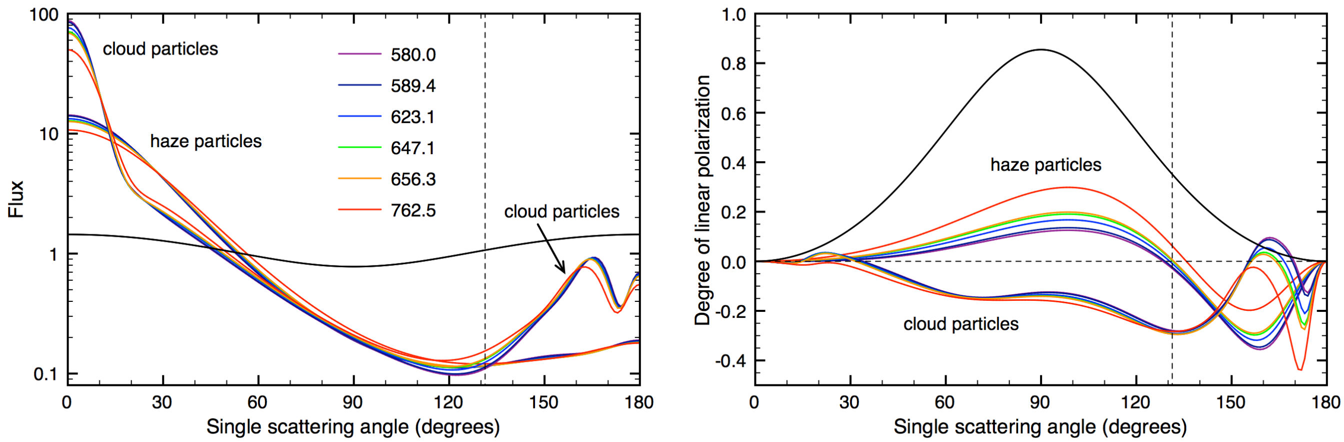

Figure 7. The flux (left) and degree of linear polarization P (right) of incident unpolarized light that is singly scattered by the cloud particles, haze particles, and gaseous molecules (solid black line) at the central wavelengths of the filters. Note that the wavelength dependence of the molecular scattering (through the depolarization factor; see Equation (10)) is so small that we show only one line. All flux curves are normalized such that their average over all scattering directions is 1.0. A positive P_s indicates a direction of polarization perpendicular to the scattering plane (the plane containing the incident and scattered light beams), and a negative P_s indicates a direction parallel to the scattering plane. The black dashed vertical lines indicate the single-scattering angle corresponding to Venus's phase angle at the time of our observations, and the black dashed horizontal line in the polarization plot indicates $P = 0$.

Table 3
The Depolarization Factor δ and the Refractive Index n of CO_2 (M. Sneep & W. Ubachs 2005), and the Molecular Scattering Optical Thickness b^m_{tot} of the Standard Model Atmosphere as a Whole at the Central Wavelength λ_0 of Each Filter (see Table 1)

Filter	λ_0 (nm)	δ	n	b^m_{tot}	σ^a_{cloud} (μm^2)	b^a_{cloud}	σ^a_{haze} (μm^2)	b^a_{haze}
Na cont.	580.0	0.0784	1.0004262	13.43	6.635	30.00	0.154	0.020
Na	589.4	0.0783	1.0004260	12.57	6.634	29.99	0.151	0.020
Sloan r	623.1	0.0779	1.0004251	9.41	6.638	30.01	0.141	0.018
Hα cont.	647.1	0.0772	1.0004246	8.59	6.650	30.06	0.134	0.017
Hα	656.3	0.0776	1.0004244	8.11	6.657	30.10	0.131	0.017
Sloan i	762.5	0.0769	1.0004228	4.41	6.928	31.32	0.104	0.014

Note. Of the b^m_{tot} of the atmosphere, 98.92% pertains to layer 1 (the bottom layer), 1.022% to layer 2, 0.000484% to layer 3, and 0.0000538% to layer 4 (the top layer). Furthermore, σ^a_{cloud} is the scattering cross section of the cloud particles, b^a_{cloud} is the optical thickness of the cloud, σ^a_{haze} is the scattering cross section of the haze particles, and b^a_{haze} is the optical thickness of the haze.

the equator aligned to the horizontal x-axis. The center of each pixel was mapped onto the spherical planet to determine the location for computing the locally reflected Stokes vector. For each pixel, we compute the Stokes vector $\boldsymbol{F}$ (see Equation (1)) of the locally reflected sunlight with wavelength λ, according to

$$\boldsymbol{F}(\lambda, \theta, \theta_0, \phi - \phi_0) = \cos\theta_0\, \boldsymbol{R}(\lambda, \theta, \theta_0, \phi - \phi_0)\, \boldsymbol{F}_0(\lambda), \tag{17}$$

where θ_0 is the local solar zenith angle, θ is the local zenith viewing angle, and $\phi - \phi_0$ is the local azimuthal difference angle (J. F. de Haan et al. 1987). Vector $\boldsymbol{F}_0$ is the incident sunlight, and $\boldsymbol{R}$ is the local planetary reflection matrix. Matrix $\boldsymbol{R}$ depends on the composition and structure of the local atmosphere and surface, and given these properties as described above, we compute it using an efficient adding–doubling algorithm (J. F. de Haan et al. 1987) that fully includes linear and circular polarization for all orders of scattering.

All angles are computed by projecting the center of each pixel onto a 3D sphere that represents Venus. Note that while θ and ϕ depend on the position of the projected center of each pixel with respect to the subobserver point on the sphere, θ_0 and ϕ_0 depend on the position of the projected center of each pixel with respect to the subsolar point, the location of which depends on Venus's phase angle α, which equaled $48\overset{\circ}{.}7$ at the time of our observations.

The reflected fluxes as computed using Equation (17) do not need further scaling because the pixels all have the same size. The lack of absolute calibration of our observed total and polarized fluxes precludes an attempt to absolutely fit the computed fluxes. The degree of polarization (Equation (2)) is a relative measure, and as such it is in principle insensitive to, e.g., changes in the air mass during the observational cycle. While the measurements by ExPo have a very high polarimetric sensitivity reaching 10^{-4} (M. Rodenhuis et al. 2012), the absolute calibration of the degree of polarization of our observations, however, is only 1%–2%. In other words, the absolute offset of the degree of polarization is on the order of 1%–2% ($P_{observed} = P_{Venus} \pm 1\%–2\%$). As we will show below, this offset does not limit our numerical simulations of the observations, as those are based on the spatial variability of P and not on its absolute value.

4. Interpreting the Ringlike Polarization Pattern

The degree and direction of polarization of sunlight reflected by a region on a planet depend strongly on the optical

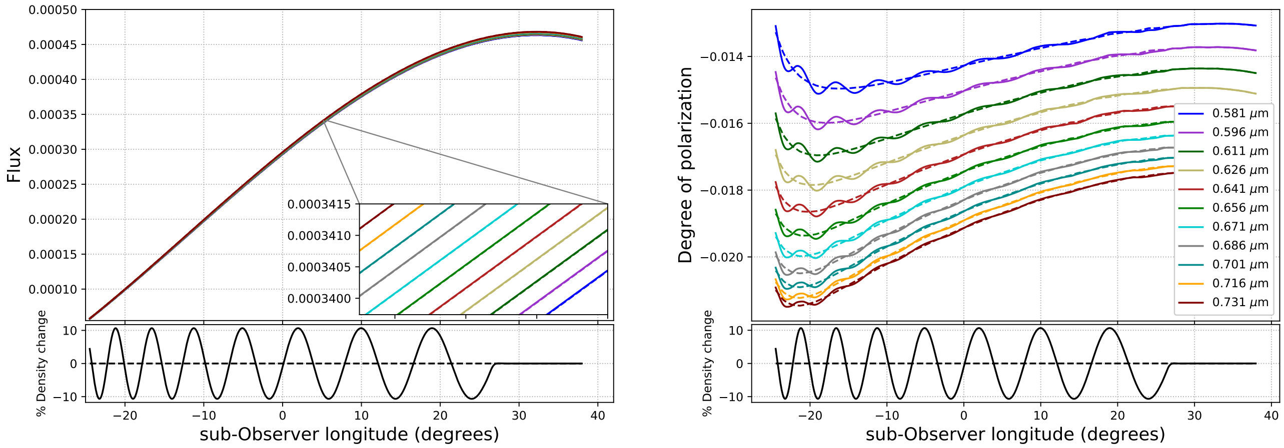

Figure 8. The total flux (left) (normalized such that at a phase angle of 0° the disk-integrated flux equals the planet's geometric albedo) and degree of linear polarization (right) along Venus's equator in response to changes in the gas column number density N^m of the upper atmospheric layer for wavelengths covered by the filters (see Table 1). The composition and structure of the lower atmospheric layers (with cloud and haze particles) are the same at every longitude. The dashed lines pertain to the baseline value of N^m, i.e., 7.0×10^{27} molecules m^{-2} (for the atmosphere up from 70 km or down to 0.036 bars). The negative sign of the degree of polarization indicates a direction parallel to the planetary scattering plane (and the equator). The empirical model shows that wave wavelengths vary gradually from about 100 km near the terminator to around 900 km near the subsolar point.

properties of the scattering particles, the illumination and viewing geometries, and the ratio of singly scattered to multiply scattered light (J. E. Hansen & L. D. Travis 1974). The singly scattered component can be highly polarized, whereas the multiply scattered component usually has a low degree of polarization. Because of the large distances between Venus and the Sun and between Venus and Earth, and given the phase angle of 48°.7, the singly scattered photons that ExPo received from locations across Venus's disk have been scattered across an angle of 131°.3. If the rings were due to variations in the microphysical properties of the scattering haze and/or cloud particles in the atmosphere, such as their size or composition, these variations should appear in a similar, concentric planet-wide pattern, and they should be small enough to virtually leave no trace in the total flux. This seems difficult to explain with our knowledge of the composition and structure of the clouds and hazes in Venus's atmosphere. The rings could also be due to variations in the local number densities of haze and/or cloud particles, as such variations would change the ratio of singly to multiple scattered light and thus the degree of polarization of the reflected light. However, the known, latitudinal variations in the cloud and haze properties (notably, cloud top altitude, N. I. Ignatiev et al. 2009; haze optical thickness, K. Kawabata et al. 1980; M. Sato et al. 1996; L. Rossi et al. 2015) seem to preclude the appearance of the concentric, planet-wide patterns.

The regularity of the polarization pattern and its apparent superposition on the high-polarization polar regions are consistent with, though do not prove, an origin in Venus's upper atmosphere. If the observed pattern is astrophysical rather than instrumental, one plausible explanation is spatial variation in the gas density above the hazes and clouds. Such planet-wide density variations could result from atmospheric waves emanating from the region close to the subsolar point, as we will discuss later. Small, local density variations in the gas above the hazes and clouds will yield small variations in the amount of locally reflected sunlight, particularly in the amount of light that has been singly scattered by gas molecules, which has a relatively high degree of polarization at a scattering angle of 131°.3 (see Figure 7 for a detailed explanation), with a direction perpendicular to the scattering plane, i.e., opposite to that of the clouds.

4.1. Numerically Reproducing the Rings

Figure 8 shows numerical simulations of the flux and degree of polarization along Venus's equator at a planetary phase angle of 48°.7. The purpose of the radiative transfer calculations is not to demonstrate that the observed pattern must be atmospheric in origin but to assess whether a physically plausible atmospheric perturbation could produce a signal of the observed type.

For the computations, we varied N^m, the gas column number density (in m^{-2}) in the highest atmospheric layer. The dashed lines in Figure 8 represent the flux and polarization of the reflected sunlight without gaseous density variations. A negative degree of polarization P_s indicates a polarization direction parallel to the scattering plane. The reflected flux appears to be virtually insensitive to variations in N^m, just like we observed. However, increasing N^m adds positive polarized flux (because of Rayleigh scattering), and thus P_s decreases, in the sense that P_s gets closer to zero. If the background P_s were positive, increasing N^m would increase P_s. Indeed, the computed variations in P_s are within ExPo's sensitivity, and even though the direction of polarization of the light scattered by the molecules is perpendicular to the reference plane and thus counteracts the polarization direction of the clouds and hazes, the direction of polarization across the variations remains parallel to the reference plane, like in the observations.

The variations in P_s are independent of the precise vertical location of the density variations, except that they should be in the upper region of the atmosphere, where the scattering is dominated by the gas. The decrease of the scattering cross section of the gas molecules with wavelength (see J. E. Hansen & L. D. Travis 1974 and Section 3) causes the decrease of the sensitivity of P_s to the density variations. This sensitivity decrease could contribute to the lack of an obvious ringlike pattern in the longer-wavelength filters, such as the Sloan *i* filter, in addition to the larger air mass and worse seeing conditions during those observations (see Table 1). We did not

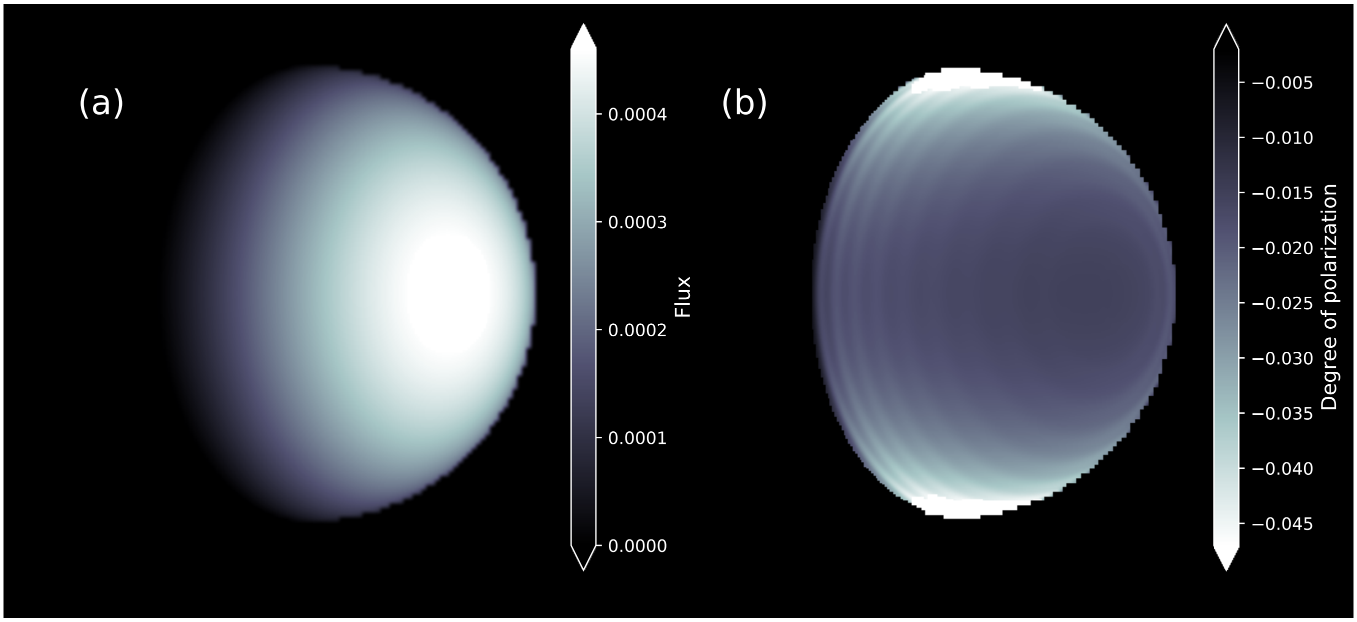

Figure 9. Numerical computations corresponding to the candidate pattern in the Hα filter ($\lambda_0 = 656$ nm), for the total flux (left) and the polarized flux (right). The background polarization signal has been subtracted from the latter. The decrease in spatial resolution due to Earth's atmosphere is not included. The planetary atmosphere is assumed to be horizontally homogeneous except for the gas-density variations.

optimize the clouds and hazes in our model atmosphere to fit the background flux and polarization in the ExPo observations, because, as mentioned earlier, the absolute accuracy of the polarization observations is limited to 1%–2%. This, however, poses no problem for our interpretation, because the absolute change in P_s due to a small change in N^m appears to be insensitive to the background polarized flux, as it adds mostly singly scattered light, which does change the reflected polarized flux but hardly changes the total flux.

Figure 9 shows numerical simulations of the total flux, degree, and direction of polarization across Venus's disk in the Hα filter, with the density variations chosen to be concentric around the region close to the subsolar point. For these simulations, the planet was assumed to be horizontally homogeneous except for the gas column number density in the upper atmospheric layer (the cloud and haze macro- and microphysical properties are thus the same everywhere).

A sinusoidal variation in the gas column number density was spatially introduced to model the effect of a density wave traveling through the upper atmosphere of Venus (see lower panels of Figure 8). The amplitude of this variation was 10% of the computed column gas density pertaining to this topmost atmospheric layer. This spatial plot illustrates that a 10% variation in the gas density of the upper atmospheric layer can produce a significant variation in P while leaving F nearly unchanged. The model wavelengths (for the rings) were chosen to span the full range of gravity-wave scales observed in Venus's atmosphere, varying from about 900 km near the subsolar (subobserver) point to 100 km near the terminator. Although empirical in nature, this choice is consistent with observations from ExPo and the Pioneer Venus mission, as well as with theoretical predictions (e.g., W. Kasprzak et al. 1988; M. Alexander 1992). More recently, the in situ Venus Express Aerodynamic Drag Experiment revealed gravity-wave activity in the planet's thermosphere (∼130–140 km), with wavelengths varying between 100 and 300 km (I. C. Müller-Wodarg et al. 2016).

5. Discussion and Conclusion

We have examined a candidate ringlike polarization pattern in a unique serendipitous ExPo dataset of Venus and explored whether such a pattern could plausibly arise from gas-density variations above the cloud tops. Similar to the observations, the modeled density variations do not leave a significant signal in the reflected total flux. If the candidate pattern is astrophysical, density perturbations of order ±10% above the cloud and haze layers (i.e., above 0.036 bars) could account for the observed polarization modulation. One possible interpretation is that such perturbations are related to previously unrecognized planet-wide atmospheric waves excited near the cloud tops about 20° (2100 km) downwind from the subsolar point (corresponding to a local time of roughly 13:00 h).

This displacement with respect to the subsolar point could be the result of a combination of a time lag in the maximum heating of the cloud layer (M. J. Belton et al. 1976) and the large equatorial wind velocities, on the order of 100 m s^{-1} (C. Counselman et al. 1980; S. S. Limaye & V. E. Suomi 1981; M. Newman et al. 1984; R. Moissl et al. 2009), that move the clouds away from the subsolar point. The waves could be propagating across the planet in the direction of the antisolar point, possibly within the known subsolar-to-antisolar flow (J. J. Goldstein et al. 1991; S. Bougher et al. 1997). According to the spatial resolution of the observations, the horizontal wavelength of the waves would be between 100 and 1000 km, decreasing with distance from the excitation region.

In situ measurements taken over 600 orbits, between about 160 and 200 km altitude, by the ONMS instrument on Pioneer Venus orbiter revealed waves (variations in gas density) in various regions on the planet (W. Kasprzak et al. 1988). These waves, with wavelengths of 100–600 km, were tentatively identified as gravity waves (H. Mayr et al. 1988). Interestingly, the Pioneer Venus measurements showed little wave activity toward the subsolar region and increasing wave activity toward the morning and evening terminators, which agrees well with

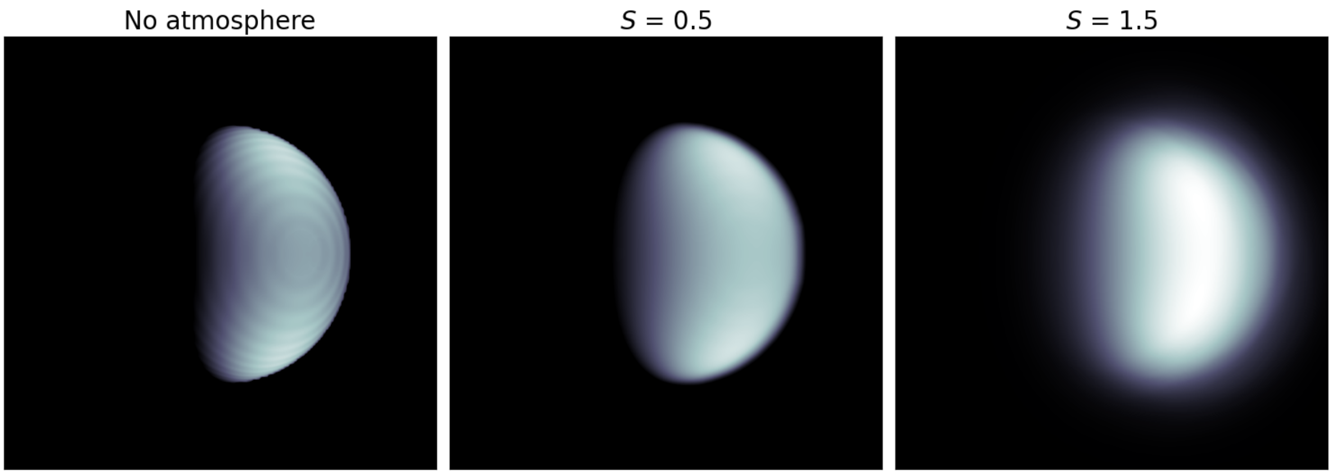

Figure 10. Numerical computations of the polarized flux Q in our Venus model in the Hα filter ($\lambda_0 = 656$ nm) after the introduction of atmospheric seeing S (arcseconds). An atmospheric phase screen is applied to the fluxes in orthogonally polarized states, which are then recombined to obtain F and Q; the signed degree of linear polarization is computed as $P_s = -Q/F$ (Equation (4)). The middle and right panels show the progressive blurring of the modeled ringlike pattern for $S = 0\farcs5$ and $S = 1\farcs5$, respectively.

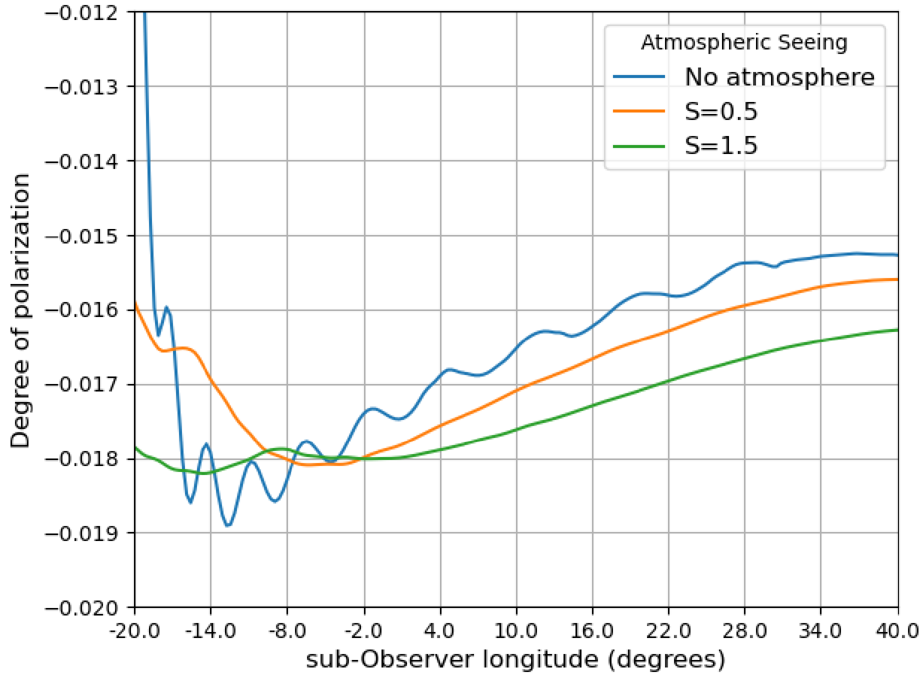

Figure 11. Illustrative 1D numerical computations of the effect of Earth atmospheric seeing S (arcseconds) on the modeled signed degree of linear polarization P_s in the Hα filter ($\lambda_0 = 656$ nm). The atmosphere is assumed to be horizontally homogeneous except for the imposed gas-density variations. Increasing S progressively attenuates the wavelike modulation in P_s. These calculations are intended to illustrate the sensitivity of the signal to seeing, not to reproduce the exact atmospheric conditions during the ExPo observations.

our ground-based observations. A planet-wide propagation was suspected for these waves (H. Mayr et al. 1988), although this could not be confirmed from Pioneer Venus's along-track data available at the time.

Because this is our only set of Venus observations with ExPo, we do not know whether the candidate pattern reflects a regularly occurring atmospheric phenomenon. If it is indeed related to the upper-atmospheric density waves observed by Pioneer Venus, it might represent a recurrent feature of Venus's atmosphere. More observations, with ground-based telescopes and/or from a future orbiter outfitted with highly sensitive polarimeters, should be performed to get insight into their appearance and variations therein. High spectral resolution polarimetry will be done by Venspec-H on ESA's EnVision mission to Venus (to be launched in 2032). However, this instrument will operate in the near-infrared, where the expected signals from such upper-atmospheric waves are weak.

Our numerical simulations (Figures 10 and 11) indicate that atmospheric blurring can substantially attenuate the polarization signal caused by the imposed gas-density variations. To explore this effect, we used an atmospheric phase screen to simulate the propagation of the incoming orthogonally polarized fluxes through Earth's atmosphere, following the approach described by D. F. Buscher (2016) and the implementation of D. Mortimer (2023). The phase screen is parameterized by the atmospheric seeing S (in arcseconds, specified at 500 nm), which controls the extent of image degradation caused by atmospheric turbulence and viewing geometry. For each value of S, the orthogonally polarized fluxes were propagated through a stochastic phase screen and then recombined to obtain the Stokes fluxes F and Q, from which we computed the signed degree of linear polarization $P_s = -Q/F$. The simulations shown here are intended to illustrate the sensitivity of the modeled ring signal to atmospheric seeing, rather than to reconstruct the exact turbulence conditions during the ExPo observations. Because the phase screens are stochastic and the detailed atmospheric conditions during the observing sequence are not known, Figures 10 and 11 should not be interpreted as defining a sharp detect/nondetect threshold. We therefore conclude only that increased air mass and degraded seeing could have contributed significantly to suppressing the visibility of the rings in the later observations.

The absence of the rings in the later Na continuum, Sloan r, and Sloan i observations is likely due to a combination of effects rather than seeing alone. In particular, the sensitivity of the polarization signal to gas-density variations decreases with wavelength because of the wavelength dependence of Rayleigh scattering, and the broad Sloan filters can further reduce the observable modulation by averaging the signal over a wider wavelength range. In addition, ExPo did not have an operational atmospheric dispersion corrector during these observations, which may have introduced spectral smearing in the broadband data. The fact that the Na image at 589.4 nm still shows clear rings, despite being taken later in the observing sequence and at higher air mass than the Hα and Hα continuum observations, further indicates that air mass alone cannot account for the detect versus nondetect behavior and is qualitatively consistent with the stronger modeled response at shorter wavelengths.

Our simulations also suggest that the degree of polarization due to the rings should be strongest at phase angles around 90° (our observations pertain to 48.°7), because the difference between the degree of polarization of light singly scattered by gaseous molecules and the background polarization is largest. To confirm the ringlike shape of the pattern, observations either at smaller phase angles than ours (where the strength of the pattern would, however, be smaller) or of Venus's morning hemisphere (our observations mostly cover the afternoon/evening hemisphere) are required. More observations, combined with an appropriate numerical model of Venus's tenuous upper atmosphere, could yield valuable insights into the physical characteristics of the waves, their surrounding environment, and their role in the planet's atmospheric dynamics.

Acknowledgments

G.M. was supported by the User Support Programme Space Research (project ALW-GO 15-37) of the Netherlands Organisation for Scientific Research (NWO). L.R. received funding from the Planetary and Exoplanetary Science (PEPSci) Programme of NWO. M.R. acknowledges support from NWO for the Extreme Polarimeter (ExPo). We thank the anonymous reviewers for their constructive comments and suggestions, which helped improve the manuscript.

ORCID iDs

Gourav Mahapatra https://orcid.org/0000-0003-2613-4413
Daphne M. Stam https://orcid.org/0000-0003-3697-2971
Loïc Rossi https://orcid.org/0000-0003-4244-3419
Christoph Keller https://orcid.org/0000-0002-1368-841X

References

Alexander, M. 1992, A Mechanism for the Venus Thermospheric Superrotation, GeoRL, 19, 2207
Alexander, M., Stewart, A., Solomon, S., & Boucher, S. 1993, Local Time Asymmetries in the Venus Thermosphere, JGR, 98, 10849
Belton, M. J., Smith, G. R., Schubert, G., & Del Genio, A. D. 1976, Cloud Patterns, Waves and Convection in the Venus Atmosphere, JAtS, 33, 1394
Bougher, S., Alexander, M., & Mayr, H. 1997, Upper Atmosphere Dynamics: Global Circulation and Gravity Waves, Venus II: Geology, Geophysics, Atmosphere, and Solar Wind Environment (Univ. Arizona Press), 259
Buscher, D. F. 2016, Simulating Large Atmospheric Phase Screens Using a Woofer-Tweeter Algorithm, OExpr, 24, 23566
Canovas, H., Rodenhuis, M., Jeffers, S., Min, M., & Keller, C. 2011, Data-Reduction Techniques for High-Contrast Imaging Polarimetry-Applications to ExPo, A&A, 531, A102
Counselman, C., Gourevitch, S., King, R., Loriot, G., & Ginsberg, E. 1980, Zonal and Meridional Circulation of the Lower Atmosphere of Venus Determined by Radio Interferometry, JGR, 85, 8026
de Haan, J. F., Bosma, P. B., & Hovenier, J. W. 1987, The Adding Method for Multiple Scattering Calculations of Polarized Light, A&A, 183, 371
de Rooij, W. A., & van der Stap, C. C. A. H. 1984, Expansion of Mie Scattering Matrices in Generalized Spherical Functions, A&A, 131, 237
Goldstein, J. J., Mumma, M. J., Kostiuk, T., et al. 1991, Absolute Wind Velocities in the Lower Thermosphere of Venus Using Infrared Heterodyne Spectroscopy, Icar, 94, 45
Hansen, J. E., & Hovenier, J. W. 1974, Interpretation of the Polarization of Venus, JAtS, 31, 1137
Hansen, J. E., & Travis, L. D. 1974, Light Scattering in Planetary Atmospheres, SSRv, 16, 527
Helbert, J., Vandaele, A. C., Marcq, E., et al. 2019, The VenSpec Suite on the ESA EnVision Mission to Venus, SPIE, 11128, 1112804
Hunten, D. M., Colin, L., Donahue, T. M., & Moroz, V. I. 2022, Venus (Univ. Arizona Press)
Ignatiev, N. I., Titov, D. V., Piccioni, G., et al. 2009, Altimetry of the Venus Cloud Tops from the Venus Express Observations, JGRE, 114, 0
Jeffers, S., Min, M., Waters, L., et al. 2012, Direct Imaging of a Massive Dust Cloud Around R Coronae Borealis, A&A, 539, A56
Kasprzak, W., Hedin, A., Mayr, H., & Niemann, H. 1988, Wavelike Perturbations Observed in the Neutral Thermosphere of Venus, JGR, 93, 11237
Kawabata, K., Coffeen, D., Hansen, J., et al. 1980, Cloud and Haze Properties from Pioneer Venus Polarimetry, JGR, 85, 8129
Kemp, J. C., Henson, G. D., Steiner, C. T., & Powell, E. R. 1987, The Optical Polarization of the Sun Measured at a Sensitivity of Parts in Ten Million, Natur, 326, 270
Kitahara, T., Imamura, T., Sato, T. M., et al. 2019, Stationary Features at the Cloud Top of Venus Observed by Ultraviolet Imager Onboard Akatsuki, JGRE, 124, 1266
Korablev, O., Fedorova, A., Bertaux, J.-L., et al. 2012, SPICAV IR Acousto-optic Spectrometer Experiment on Venus Express, P&SS, 65, 38
Lee, Y. J. 2024, Long-term Monitoring Plan of Venus using Earth-orbiting CubeSats, EPSC, 17, 158
Limaye, S. S., & Suomi, V. E. 1981, Cloud Motions on Venus: Global Structure and Organization, JAtS, 38, 1220
Mayr, H., Harris, I., Kasprzak, W., Dube, M., & Varosi, F. 1988, Gravity Waves in the Upper Atmosphere of Venus, JGR, 93, 11247
Migliorini, A., Altieri, F., Zasova, L., et al. 2011, Oxygen Airglow Emission on Venus and Mars as Seen by VIRTIS/VEX and OMEGA/MEX Imaging Spectrometers, P&SS, 59, 981
Min, M., Jeffers, S. V., Canovas, H., et al. 2013, The Color Dependent Morphology of the Post-AGB Star HD 161796, A&A, 554, A15
Moissl, R., Khatuntsev, I., Limaye, S., et al. 2009, Venus Cloud Top Winds from Tracking UV Features in Venus Monitoring Camera images, JGRE, 114, E00B31

Mortimer, D. 2023, Telescope Simulator, GitHub, https://github.com/dmortimer101/Telescope_Simulator
Müller-Wodarg, I. C., Bruinsma, S., Marty, J.-C., & Svedhem, H. 2016, In Situ Observations of Waves in Venus's Polar Lower Thermosphere with Venus Express Aerobraking, NatPh, 12, 767
Neefs, E., Vandaele, A. C., De Cock, R., et al. 2025, VenSpec-H spectrometer on the ESA EnVision mission: Design, modeling, analysis, AcAau, 226, 178
Newman, M., Schubert, G., Kliore, A. J., & Patel, I. R. 1984, Zonal Winds in the Middle Atmosphere of Venus from Pioneer Venus Radio Occultation Data, JAtS, 41, 1901
Peralta, J., Hueso, R., Sánchez-Lavega, A., et al. 2017, Stationary Waves and Slowly Moving Features in the Night Upper Clouds of Venus, NatAs, 1, 0187
Persson, M., Wilson, C. F., Grotheer, E., et al. 2026, Densities of the Venusian Thermosphere as Revealed by Venus Express Torque Data, Icar, 457, 117163
Piccialli, A., Titov, D. V., Sanchez-Lavega, A., et al. 2014, High Latitude Gravity Waves at the Venus Cloud Tops as Observed by the Venus Monitoring Camera on Board Venus Express, Icar, 227, 94
Rodenhuis, M., Canovas, H., Jeffers, S., et al. 2012, The Extreme Polarimeter: Design, Performance, First Results and Upgrades, in Ground-based and, SPIE, 8446, 1413
Rodenhuis, M., Canovas, H., Jeffers, S., & Keller, C. 2008, The Extreme Polarimeter (ExPo): Design of a Sensitive Imaging Polarimeter, SPIE, 7014, 70146T
Rodenhuis, M., & Keller, C. U. 2007, Design Options for the Extreme Polarimeter (ExPo), in Proc. Conf. Spirit of Bernard Lyot: The Direct Detection of Planets and Circumstellar Disks in the 21st Century, ed. P. Kalas, 43
Rossi, L., Marcq, E., Montmessin, F., et al. 2015, Preliminary Study of Venus Cloud Layers with Polarimetric Data from SPICAV/VEx, P&SS, 113, 159
Rossi, L., & Stam, D. M. 2018, Circular Polarization Signals of Cloudy (Exo) Planets, A&A, 616, A117
Sato, M., Travis, L., & Kawabata, K. 1996, Photopolarimetry Analysis of the Venus Atmosphere in Polar Regions, Icar, 124, 569
Sneep, M., & Ubachs, W. 2005, Direct Measurement of the Rayleigh Scattering Cross Section in Various Gases, JQSRT, 92, 293
Stam, D., De Haan, J., Hovenier, J., & Stammes, P. 1999, Degree of Linear Polarization of Light Emerging from the Cloudless Atmosphere in the Oxygen A Band, JGR, 104, 16843
Travis, L. D. 1979, Imaging and Polarimetry with the Pioneer Venus Orbiter Cloud Photopolarimeter, SPIE, 183, 299